

4

DTIC FILE COPY

Saturation Broadening by Inhomogeneous Fields

AD-A214 544

J. C. CAMPARO
Chemistry and Physics Laboratory
Laboratory Operations
The Aerospace Corporation
El Segundo, CA 90245

31 July 1989

Prepared for

SPACE SYSTEMS DIVISION
AIR FORCE SYSTEMS COMMAND
Los Angeles Air Force Base
P.O. Box 92960
Los Angeles, CA 90009-2960

APPROVED FOR PUBLIC RELEASE;
DISTRIBUTION UNLIMITED

DTIC
ELECTE
NOV 24 1989
S B D

89 11 21 147

This report was submitted by The Aerospace Corporation, El Segundo, CA 90245, under Contract No. F04701-85-C-0086-P00019 with the Space Systems Division, P. O. Box 92960, Los Angeles, CA 90009-2960. It was reviewed and approved for The Aerospace Corporation by S. Feuerstein, Director, Chemistry and Physics Laboratory.

Capt Mitchell was the Air Force project officer for the Mission-Oriented Investigation and Experimentation (MOIE) Program.

This report has been reviewed by the Public Affairs Office (PAS) and is releasable to the National Technical Information Service (NTIS). At NTIS, it will be available to the general public, including foreign nationals.

This technical report has been reviewed and is approved for publication. Publication of this report does not constitute Air Force approval of the report's findings or conclusions. It is published only for the exchange and stimulation of ideas.

Michael J Mitchell
MICHAEL MITCHELL, CAPT, USAF
MOIE Project Officer
SSD/CWNZ

Raymond M Leong
RAYMOND LEONG, MAJ, USAF
MOIE Program Manager
AFSTC/WCO OL-AB

REPORT DOCUMENTATION PAGE

1a. REPORT SECURITY CLASSIFICATION Unclassified			1b. RESTRICTIVE MARKINGS		
2a. SECURITY CLASSIFICATION AUTHORITY			3. DISTRIBUTION/AVAILABILITY OF REPORT Approved for public release; distribution unlimited.		
2b. DECLASSIFICATION/DOWNGRADING SCHEDULE					
4. PERFORMING ORGANIZATION REPORT NUMBER(S) TR-0088(3945-05)-1			5. MONITORING ORGANIZATION REPORT NUMBER(S) SSD-TR-89-86		
6a. NAME OF PERFORMING ORGANIZATION The Aerospace Corporation Laboratory Operations		6b. OFFICE SYMBOL (if applicable)	7a. NAME OF MONITORING ORGANIZATION Space Systems Division		
6c. ADDRESS (City, State, and ZIP Code) El Segundo, CA 90245			7b. ADDRESS (City, State, and ZIP Code) Los Angeles Air Force Base Los Angeles, CA 90009-2960		
8a. NAME OF FUNDING/SPONSORING ORGANIZATION		8b. OFFICE SYMBOL (if applicable)	9. PROCUREMENT INSTRUMENT IDENTIFICATION NUMBER F04701-85-C-0086-P00019		
8c. ADDRESS (City, State, and ZIP Code)			10. SOURCE OF FUNDING NUMBERS		
			PROGRAM ELEMENT NO.	PROJECT NO.	TASK NO.
					WORK UNIT ACCESSION NO.
11. TITLE (Include Security Classification) Saturation Broadening by Inhomogeneous Fields					
12. PERSONAL AUTHOR(S) Camparo, James C.					
13a. TYPE OF REPORT		13b. TIME COVERED FROM _____ TO _____		14. DATE OF REPORT (Year, Month, Day) 1989 July 31	
15. PAGE COUNT 27					
16. SUPPLEMENTARY NOTATION					
17. COSATI CODES			18. SUBJECT TERMS (Continue on reverse if necessary and identify by block number)		
FIELD	GROUP	SUB-GROUP	Atomic Clocks Rubidium Frequency Standards		
			Magnetic Resonance Saturation Broadening		
			Optical Pumping		
19. ABSTRACT (Continue on reverse if necessary and identify by block number) According to the standard Karplus-Schwinger theory of saturation broadening, saturated line shapes are Lorentzians with linewidths that increase linearly with the perturbing field strength. This, however, is not what is observed experimentally when the saturating field is inhomogeneous. If the saturating field strength varies significantly over the experimental signal volume, we find that the saturated line shapes are strikingly non-Lorentzian. The "sharpness" of the experimental line shapes is quantified by an "effective linewidth," which is the half width at half maximum of a Lorentzian that approximates the experimental line shape near line center. For certain classes of inhomogeneous fields, we find that this effective linewidth increases approximately as the square root of the saturating field strength, rather than linearly. We show that this class of inhomogeneous fields is distinguished by the presence of a node in the field geometry, and that the effect arises because the line shape near line center is dominated by the atomic population in the vicinity of the node. These results indicate the importance of understanding and accounting for inhomogeneous field effects when extracting physical information from experimental line shapes.					
20. DISTRIBUTION/AVAILABILITY OF ABSTRACT <input type="checkbox"/> UNCLASSIFIED/UNLIMITED <input checked="" type="checkbox"/> SAME AS RPT. <input type="checkbox"/> DTIC USERS			21. ABSTRACT SECURITY CLASSIFICATION Unclassified		
22a. NAME OF RESPONSIBLE INDIVIDUAL			22b. TELEPHONE (Include Area Code)		22c. OFFICE SYMBOL

PREFACE

The author would like to thank Dr. R. Frueholz and Dr. B. Jaduszliwer for critical readings of the manuscript, and S. Delcamp for help in performing the experiments.

Session For	
DTIC GRA&I	<input checked="checked" type="checkbox"/>
DTIC TAB	<input type="checkbox"/>
Unannounced	<input type="checkbox"/>
Justification	
By	
Distribution/	
Availability Codes	
Dist	Avail and/or Special
A-1	

CONTENTS

PREFACE	1
I. INTRODUCTION	7
II. EXPERIMENT	9
III. NUMERICAL SIMULATION	17
IV. ANALYTIC APPROXIMATION	23
V. SUMMARY	29
REFERENCES	31

FIGURES

1.	(a) Experimental Arrangement; (b) Pertinent Energy Levels of ^{87}Rb	10
2.	Spatial Variations of the Microwave Magnetic Field's Axial Component (F_z)	11
3.	(a) Experimental Saturated Line Shape Obtained from the TE_{111} Mode Field Geometry; (b) Lorentzian Line Shape of the Same Half-Width Half-Maximum (HWHM)	13
4.	Plot of the Experimental HWHM ($\Delta\nu$) and Effective Linewidth ($\delta\nu$) vs Average Field Strength (F)	14
5.	Theoretical Line Shapes for Three Different Values of the Microwave Power Supplied to a TE_{111} Cavity Mode	18
6.	Plot of the Theoretical HWHM ($\Delta\nu$) and Effective Linewidth ($\delta\nu$) vs the Average Field Strength (F)	20
7.	Plot of the Theoretical HWHM ($\Delta\nu$) and Effective Linewidth ($\delta\nu$) vs the Average Field Strength (F)	22
8.	(a) One-dimensional Field Geometry Used in the Analytic Analysis of Saturation Broadening by Inhomogeneous Fields; (b) Energy-level Diagram of the Simple Two-level Quantum System Used in the Analytic Analysis	24

I. INTRODUCTION

In the mid to late 1940s, Townes,¹ Karplus, and Schwinger,² and Snyder and Richards³ were concerned with the problem of collision broadening in the presence of intense electromagnetic radiation fields, and as a result initiated the study of saturation- (or power-) broadened resonance line shapes.⁴ Working in the impact approximation for the collision process, Karplus and Schwinger showed that though resonance line shapes retain their Lorentzian character in the presence of strong fields, the width of the Lorentzian will be larger than that expected from relaxation alone. Defining $\Delta\nu$ as the resonance linewidth [half-width at half maximum (HWHM)], Karplus and Schwinger obtained a simple relationship between the linewidth and the field-atom interaction strength,

$$\Delta\nu = [\gamma^2 + (\mu F/\hbar)^2]^{1/2}. \quad (1)$$

Here μ is a transition matrix element, F is the field strength, and γ is the quantum system's relaxation (dephasing) rate.

As a consequence of the Lorentzian character of the Karplus-Schwinger line shape, the saturation-broadened linewidth provides a good measure of "line-shape sharpness," and hence a good estimate of the spectroscopic ability to find a saturated resonance's center frequency. Though the actual measure of line-shape sharpness is the line shape's second derivative evaluated at the resonance frequency, in the case of a Lorentzian it is quite easy to show that

$$\Delta\nu = \sqrt{-2S(\nu_0)/S''(\nu_0)}, \quad (2)$$

where $S(\nu_0)$ is the signal amplitude at the resonance frequency ν_0 and $S''(\nu_0)$ is the corresponding value of the second derivative. Thus, since saturation-broadened line shapes are expected to retain their Lorentzian character, the Karplus-Schwinger linewidth formula, Eq. (1), has the spectroscopic implication that in the saturation regime, the ability to find a resonance's center frequency decreases inversely to the field strength, i.e., $[S''(\nu_0)]^{1/2} \sim 1/F$.

In recent years, some of the interest in saturation-broadened line shapes has been directed towards extending the theory of collision broadening in strong fields to situations where the impact approximation is not valid,^{5,6} and experimentally verifying the Karplus-Schwinger linewidth formula in the optical regime.⁷ There has also, however, been considerable interest in extending experimental research into regimes where the assumptions of the Karplus-Schwinger theory may be only marginally valid. For example, power broadening has been examined in regimes where the radiation field bandwidth is non-negligible.⁸ Additionally, deviations from the Karplus-Schwinger linewidth formula have been observed in solids;⁹ they have been observed when the dephasing rate $1/T_2$ is not equal to the longitudinal relaxation rate $1/T_1$;¹⁰ and they have been observed when the quantum system has more than just two levels.¹¹

A significant assumption in the Karplus-Schwinger theory is homogeneity of the field over the experimental signal volume. However, for the real fields employed in the laboratory, this

assumption is never rigorously satisfied. Hence, a question arises as to the shape of saturated resonances when this assumption is relaxed; specifically, when the field shows significant inhomogeneity over the signal volume. This question is of more than just academic interest, since the magnetic resonance signal of atomic clocks and masers is often stimulated by a specific microwave-cavity mode. In the present study, we therefore relax the assumption of field homogeneity, and examine the resulting non-Lorentzian character of saturation-broadened resonances.

In the following sections, attention will focus on the spectroscopically important relationship between the average saturating field strength and line-shape sharpness. In Section II, an experiment examining the saturated line shape of an atom confined in the inhomogeneous field of a microwave cavity will be described. As will be shown, the saturated line shapes obtained in this experiment differ markedly from the Lorentzian line shapes expected from the Karplus-Schwinger theory. Then in Section III, the results from a numerical simulation of the experiment and its cavity mode field geometry will be presented and discussed, as well as simulations of experiments employing other types of field geometries. The results from these calculations will highlight those spatial properties of the field that have a primary influence on the shape of the saturated resonance. Finally, in Section IV, using the conclusions of the previous sections, we will present an approximate analytic solution to the problem of a saturated resonance's line shape. The purpose of this section will be to gain physical insight into why the saturated atomic resonance displays a non-Lorentzian shape.

II. EXPERIMENT

In order to examine saturation broadening in the presence of inhomogeneous electromagnetic fields, at least two conditions must be present in the experimental design. Obviously, it is necessary that the field exhibit sufficient inhomogeneity in order that the field's spatial variations are manifested in the observed line shape. Additionally, it is necessary that the atomic motion be "slow" so that the atoms do not motionally average the field inhomogeneities. Both of these conditions can be met in experiments examining the 0-0 hyperfine transition line shape in optically pumped alkali-metal vapors. Additionally, as a result of Dicke narrowing,¹² Doppler broadening does not confound the experimental results.

The experimental arrangement is shown schematically in Figure 1. Light from a Mitsubishi ML-4102 single-mode diode laser,¹³ tuned to the D_2 resonance of Rb at 780.2 nm, was allowed to pass through a ~ 1 cm orifice in the front face of a microwave cavity and into an atomic resonance cell. The total output power of the laser at the D_2 resonance was 2.5 mW, and it had a single-mode linewidth (full width at half-maximum) of 44 MHz. Additionally, in an attempt to probe atoms throughout the cavity volume, the beam was made to diverge after passing through a lens; a beam diffusing element was placed over the cavity orifice, and a photodiode for detecting the transmitted light was placed inside the cavity. (The sensitive area of the diode was approximately equal to the cross-sectional area of the cavity.) By centering the cavity and resonance cell in a pair of Helmholtz coils, which produced an axial static magnetic field of several gauss, the ground-state Zeeman degeneracy was lifted so that only the $(m_F = 0) - (m_F = 0)$ hyperfine transition was resonant with the cavity's microwave field.

A vapor of natural Rb (28% ^{87}Rb and 72% ^{85}Rb) in equilibrium with a droplet of liquid metal at approximately 64°C was contained in a cylindrical Pyrex resonance cell along with 100 torr of N_2 . The nitrogen was present in order to both reduce the contribution of wall collisions to the atomic system's relaxation rate,¹⁴ and to limit motional averaging of the field. The resonance cell was placed inside a microwave cavity whose TE_{111} mode was resonant with the ^{87}Rb 0-0 ground-state hyperfine transition. The spatial variation of the TE_{111} mode's axial magnetic field component, which is the field component responsible for exciting the 0-0 transition, is given by¹⁵

$$F_z(r, \phi, z) = F_0 J_1(1.841r/R) \cos(\phi) \sin(\pi z/L), \quad (3)$$

where $J_1(x)$ is a first-order Bessel function, R is the cavity radius, and L its length; the radial and angular variations of this field mode are illustrated in Figure 2. This particular cavity mode was chosen because the field geometry has a nodal plane, which is a condition of significant field inhomogeneity. As a result of the high nitrogen density, motional averaging of the field inhomogeneity was negligible. Under the experimental conditions, the atomic diffusion coefficient D had the value $1.4 \text{ cm}^2/\text{sec}$,¹⁶ so that the rms atomic spatial displacement δl was estimated as 0.17 cm [assuming a 10 msec dephasing time T_2 and taking $\delta l = (2DT_2)^{1/2}$]; this is to be compared with the microwave cavity's 2.7 cm diameter and 3.8 cm length.

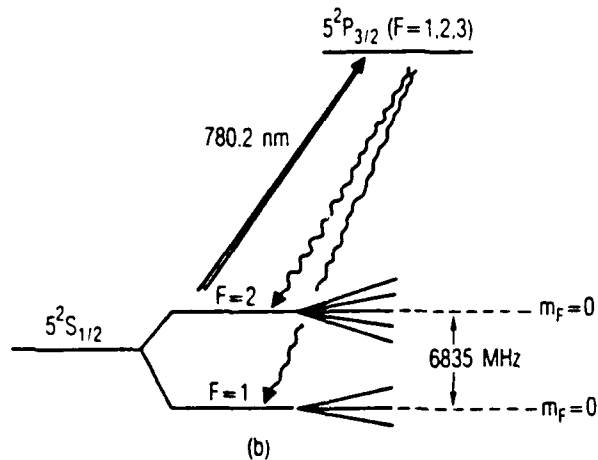
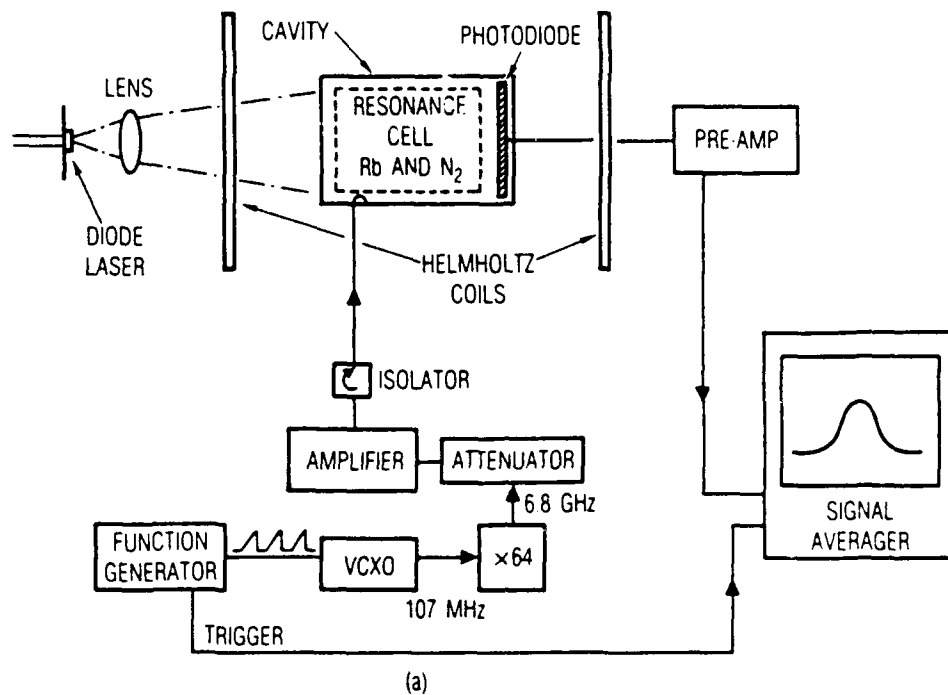


Figure 1. (a) Experimental arrangement. A diode laser optically pumps ^{87}Rb atoms contained in a Pyrex glass resonance cell. The resonance cell is located inside a microwave cavity whose TE_{111} mode is resonant with the alkali-metal-atom's ground-state 0-0 hyperfine transition. The microwaves are supplied to the cavity through the chain of rf multiplication and amplification shown in the figure. (b) Pertinent energy levels of ^{87}Rb . Depopulation optical pumping creates a population imbalance (i.e., hyperfine polarization) between the alkali-metal ground-state hyperfine manifolds, which is perturbed by the strong microwave field at ~ 6835 MHz.

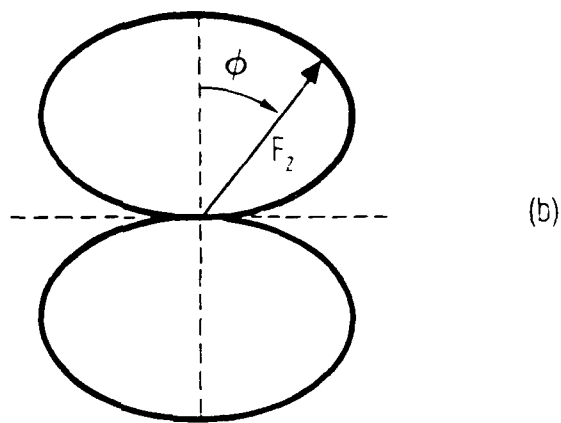
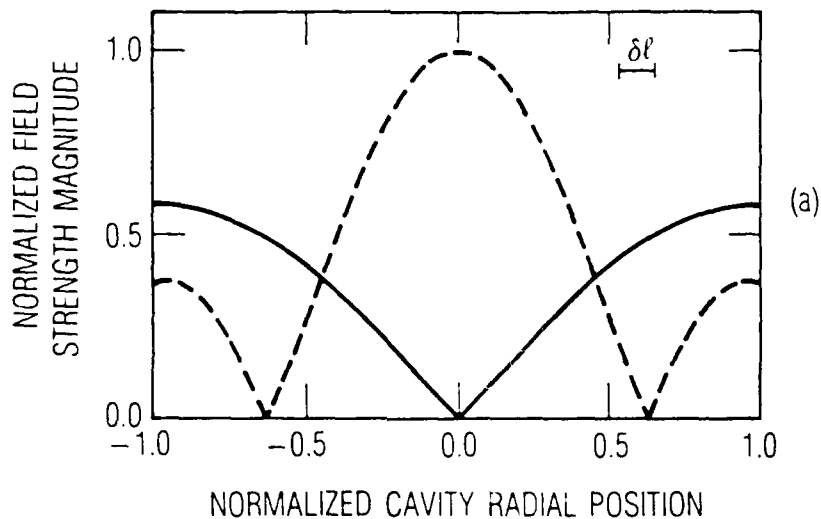


Figure 2. Spatial variations of the microwave magnetic field's axial component (F_z). This component of the electromagnetic field is responsible for the transitions between the $m_F = 0$ Zeeman sublevels of the alkali-metal ground state. (a) radial variation of $|F_z|$ for both a TE_{111} cavity mode (solid line) and a TE_{011} cavity mode (dashed line). For illustrative purposes, the relative rms atomic spatial displacement δl , discussed in the text, is also shown. (b) Polar plot showing the variation of F_z with azimuthal angle ϕ for a TE_{111} cavity mode. The TE_{011} mode has azimuthal symmetry, so there is no ϕ dependence.

Microwave power was supplied to the cavity through the chain of rf multiplication and amplification shown in Figure 1(a). Since the power entering the cavity is proportional to the stored energy in the cavity,¹⁵ the attenuators placed in the microwave path could be used to vary the magnitude of the average field strength in a well defined manner. Additionally, the frequency of the approximately 106.8 MHz rf coming from the voltage-controlled oscillator was ramped by a function generator, so that the microwave frequency swept slowly over the 0-0 hyperfine transition.

By tuning the diode laser to the D_2 ^{87}Rb transition [$5^2P_{3/2}(F=1,2,3)-5^2S_{1/2}(F=2)$], the atomic population in the $F=2$ ground-state hyperfine manifold was transferred by depopulation optical pumping into the $F=1$ ground-state hyperfine manifold.¹⁴ In the absence of microwaves at the appropriate frequency, this resulted in a maximum for the light intensity transmitted through the resonance cell. As the microwaves swept over the 0-0 hyperfine transition at 6835 MHz, atoms in the ($F=1, m_F=0$) Zeeman sublevel returned to the ($F=2, m_F=0$) Zeeman sublevel, with the effect of reducing the transmitted laser intensity. Since the atoms were locally confined by the nitrogen buffer gas, the change in transmitted light intensity associated with any particular region of the vapor depended upon the local field strength in that region, and the region's initial (equilibrium) population imbalance due to optical pumping. The observed change in transmitted laser intensity thus mapped out the full signal volume's 0-0 hyperfine transition line shape as the microwave frequency was scanned across the hyperfine resonance, and this line shape was recorded with a signal averager.

An example of a saturated line shape obtained in this experiment is shown in Figure 3(a). Since the intrinsic HWHM of the transition under the experimental conditions was ~ 1 kHz, the observed ~ 25 kHz HWHM for this experimental line shape implies a condition of extreme saturation broadening. For comparative purposes, the figure also shows a Lorentzian line shape with the same HWHM as the experimental line shape, and it is clear even visually that the experimental line shape deviates significantly from a Lorentzian. Specifically, the experimental line shape appears to be sharper than a Lorentzian of the same linewidth. In order to quantify the relative sharpness of the observed saturated resonances, we define an "effective linewidth" $\delta\nu$ which is related to the resonance line shape's second derivative through Eq. (2) [$S''(\nu_0)$ was obtained from the line-shape data stored in the signal averager by numerical differentiation]. In essence $\delta\nu$ is the linewidth of the Lorentzian that approximates the experimental line shape near line center, so that in regimes where the Karplus = Schwinger theory is valid, one would have $\Delta\nu = \delta\nu$.

The results of this analysis are shown in Figure 4, where the effective linewidth ($\delta\nu$) and the HWHM ($\Delta\nu$) are plotted as a function of the average field strength in the microwave cavity. The straight lines represent least-squares fits to the data, assuming a power-law scaling relation between linewidth and field strength

$$\Delta\nu \propto (F)^a \quad (4a)$$

and

$$\delta\nu \propto (F)^b. \quad (4b)$$

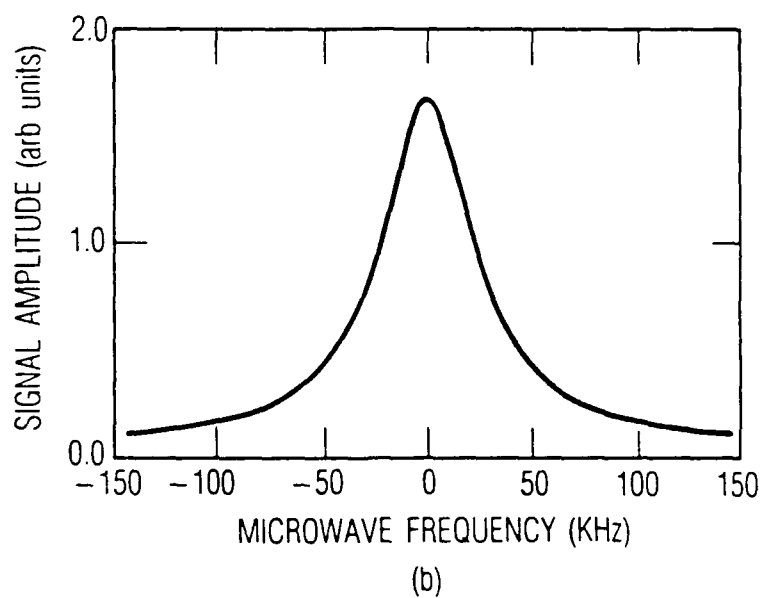
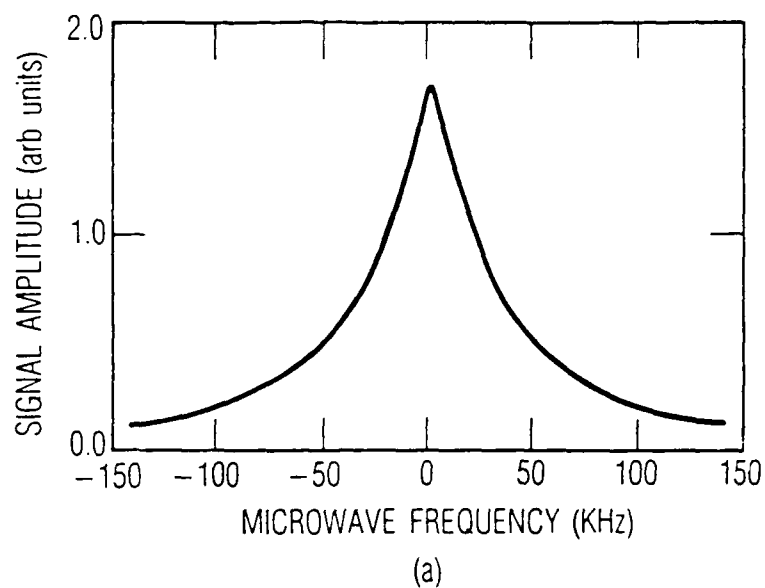


Figure 3. (a) Experimental saturated line shape obtained from the TE_{111} mode field geometry. (b) Lorentzian line shape of the same half-width half-maximum (HWHM). It is clear that the saturated line shapes obtained with the inhomogeneous field differ significantly from the Lorentzians predicted by the Karplus-Schwinger theory.

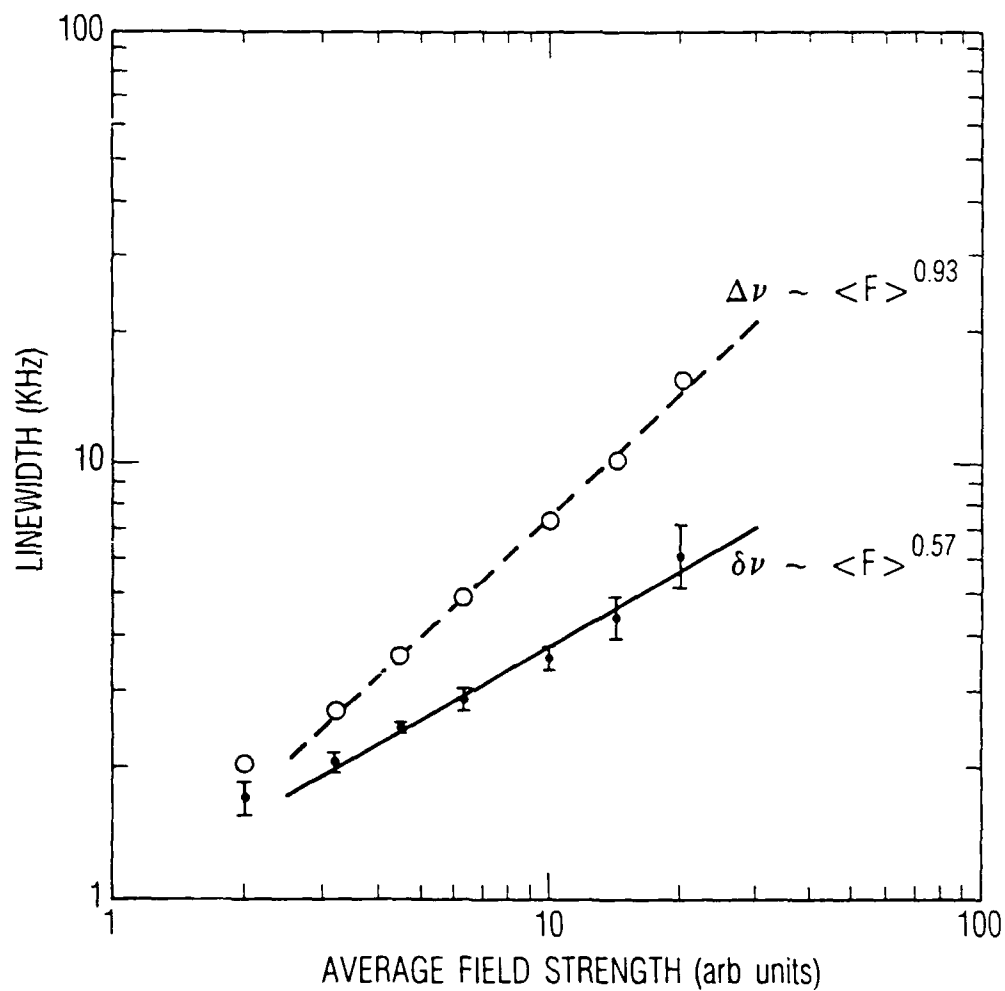


Figure 4. Plot of the experimental HWHM ($\Delta\nu$) and effective linewidth ($\delta\nu$) vs average field strength $\langle F \rangle$. The data were fit to power-law scaling relations to determine the values of the exponents shown in the figure.

Since a power-law relation should only be valid when the intrinsic width of the saturated resonance is negligible, the lowest field strength data were excluded from the analysis (since the intrinsic linewidth must be less than or equal to this value).

The data of Figure 4 support the previous qualitative conclusion that the observed line shape is sharper than a Lorentzian of the same half-width. This is illustrated in Figure 4 by the fact that the effective linewidth is always smaller than the HWHM. Additionally, the data show that the HWHM and the effective linewidth increase at different rates as the magnitude of the average field strength increases. As evidenced by the values of α and β given in the figure, it appears that the HWHM increases in a nearly linear fashion with the field strength ($\alpha \sim 1$), consistent with the Karplus-Schwinger theory, while the effective linewidth exhibits a square-root dependence on field strength magnitude ($\beta \sim 1/2$).

Naively, these results might be taken as strong evidence that field inhomogeneity has a pronounced effect on the saturation-broadening behavior of experimental line shapes. However, it is important to mention that the high nitrogen density used in this experiment has a further consequence for the observed line shape. It is well known that as a result of the strongly relaxing glass surface, the presence of a buffer gas results in spatial modes for the population imbalance between the two hyperfine manifolds.¹⁷ Consequently, not all spatial regions within the field contribute to the observed line shape to the same degree. Hence, the experimentally observed line shape is a manifestation of *two* inhomogeneities: one due to the field, and the other due to the equilibrium population imbalance (i.e., the population imbalance between the two states in the absence of the microwave field). At this point in the discussion, we can only suggest that the observed saturation-broadening behavior is associated with the field's inhomogeneity. In the next section we will address this problem with a series of numerical simulations of the experiment. Our method will be to unravel the various spatial variations that might give rise to this behavior, and to see separately the effect of each on the macroscopic line shape.

III. NUMERICAL SIMULATION

The numerical simulation of the preceding 0-0 hyperfine transition line-shape experiment has been extensively discussed in previous publications.¹⁸⁻²¹ Therefore, only a brief description of the simulation, highlighting some of its salient features, will be given here. In the calculations the relevant gas-phase physics occurs on two different scales. On the microscopic scale, the line shape is determined by the generalized Vanier theory.¹¹ This density-matrix theory describes the multi-Zeeman level optical pumping process which results in the alkali-metal hyperfine polarization (i.e., the population imbalance between the two hyperfine manifolds), and yields a Lorentzian 0-0 hyperfine transition line shape, with a HWHM that depends on the field strength in a fashion analogous to Eq. (1).²² However, since atoms in different regions of the cavity experience different microwave-field strengths, and since atomic diffusion through the molecular buffer gas yields spatial modes of hyperfine polarization,¹⁷ the microscopic response to the field varies on the macroscopic scale of the field's and polarization's spatial distributions.

In practice the observed (macroscopic) line shape is calculated by dividing the cylindrical cavity volume into thousands of small tubes, minimally 4300, and calculating the total optical power transmitted by these tubes as a function of microwave frequency. The tubes are chosen to have a small diameter so that variations of field strength and hyperfine polarization across the tube face are not appreciable. Thus, for an individual tube, the only spatial variation in either the field or the hyperfine polarization is an axial one. Each tube is associated with an appropriately normalized field strength value, so that any particular transverse geometry for the field may be considered in the calculations. To account for the transverse spatial distribution of hyperfine polarization, an appropriate weighting function is superimposed onto the generalized Vanier theory solutions for each tube. For a given microwave detuning from resonance, and a given microwave field energy in the cavity, the optical power transmitted through each tube is determined by assuming a Bouguer-Beer-Lambert law for optical attenuation: $I \sim I_0 \exp(-[N]\sigma L)$.²³ Here, $[N]$ is the average number density of absorbers in the tube of length L , which is a function of the axial distribution of microwave-field strength and hyperfine polarization. The optical powers transmitted by the tubes are then summed, which yields the observed signal amplitude for the specific microwave frequency detuning from resonance.

Considering the cases of a TE₁₁₁ cavity mode, and using other parameters appropriate to the previously described experiment, Figure 5 provides several examples of calculated line shapes for differing values of the average cavity mode field strength $\langle F \rangle$. (Nearly all the parameters required by the numerical simulation are measured; the only free parameters in the calculations are the microwave power entering the cavity and the cavity Q .) It is clear that as the average field strength increases, the HWHM increases, as observed experimentally. Additionally, for increasing values of $\langle F \rangle$, the line shapes display a growing deviation from the Karplus-Schwinger Lorentzian character. In particular, at the very highest value of $\langle F \rangle$, the resonance has a cusplike appearance, implying that the second derivative of this line shape is comparatively large, given its HWHM (i.e., $\delta\nu \ll \Delta\nu$).

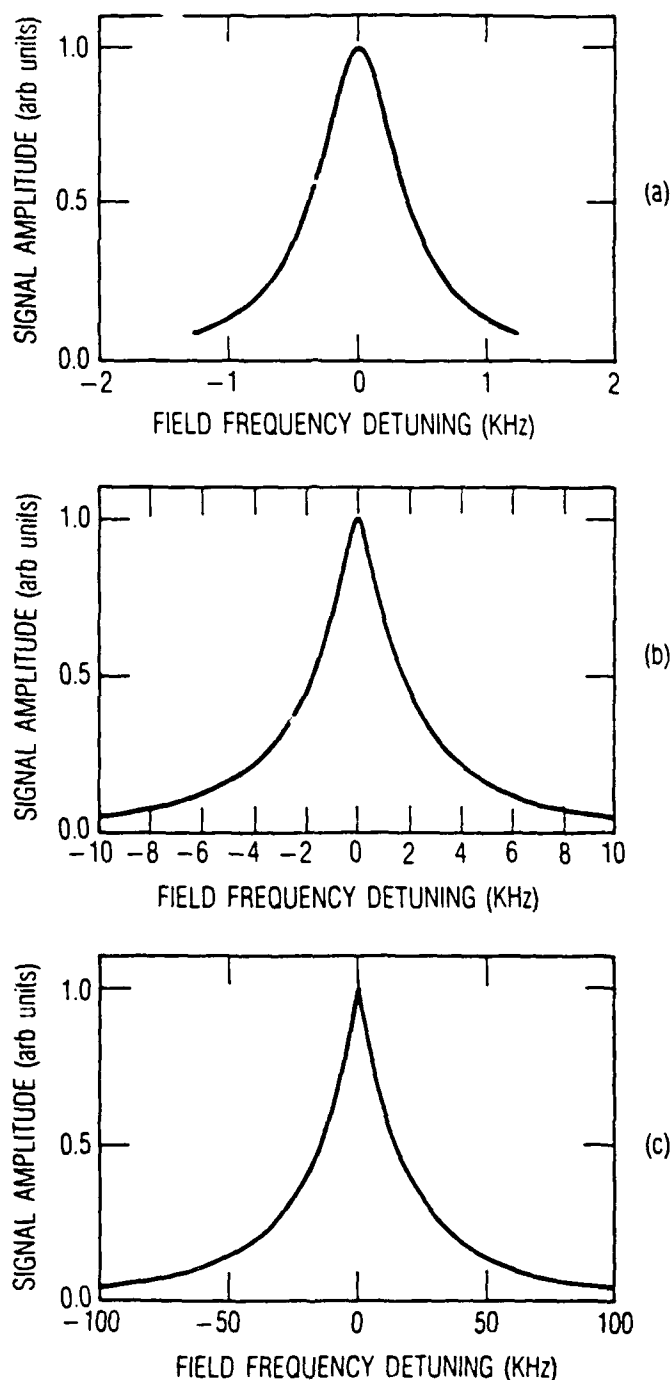


Figure 5. Theoretical line shapes for three different values of the microwave power supplied to a TE_{111} cavity mode (cavity Q was set equal to 100). (a) Microwave power is 0.001 mW, (b) microwave power is 0.1 mW, and (c) microwave power is 10.0 mW. Since the average field strength in the cavity is proportional to the square root of the power, (a)-(c) represent a factor of 100 change in the average field strength. Note that as the average field strength increases, the line shapes exhibit an increasing deviation from a Lorentzian shape.

To quantify the growing non-Lorentzian character of the saturated resonances, Figure 6 shows the calculated HWHM and effective linewidth as a function of average field strength. The solid lines correspond to least-squares fits of the numerical data, and give exponents for the power-law scaling relations. Comparing Figures 4 and 6, it is clear that there is reasonably good agreement between theory and experiment. In particular, the theoretical HWHM shows a nearly linear dependence on field strength, while the effective linewidth shows an approximately square-root dependence on field strength.

These theoretical results indicate that the source of the line-shape's non-Lorentzian character is properly modeled by some portion of the numerical simulation. Therefore, by examining the simulation's predictions under alternate "fictitious" conditions, where the various spatial distributions are eliminated one by one, it should be possible to uncover this portion of the numerical simulation, and hence the source of the observed line shape behavior. With this as a goal, several sets of calculations were thus performed. In the first set, we considered the same experiment, except that the axial field component of the TE_{111} mode was only allowed to exhibit an angular and axial spatial variation [i.e., we removed the radial dependence of the field from the calculations so that $F_z(r, \phi, z) \rightarrow F_z(\phi, z)$]. Similarly, in the second set, we only allowed the field of the TE_{111} mode to vary along its radial and axial dimensions [i.e., we removed the angular dependence of the field from the calculations so that $F_z(r, \phi, z) \rightarrow F_z(r, z)$]. Then in the third set, we removed both the radial and angular field variations from the calculations, so that the field of the TE_{111} mode had only an axial spatial variation [i.e., $F_z(r, \phi, z) \rightarrow F_z(z)$]. In all of the calculations, the spatial distribution of hyperfine polarization was the same as that used in the previous TE_{111} mode simulation of the experiment.

The power-law exponents obtained from these fictitious simulations are collected in Table I, while Figure 7 shows both $\delta\nu$ and $\Delta\nu$ as a function of average field strength for the $F_z(\phi, z)$ and $F_z(z)$ calculations. The dashed-dotted line and circles correspond to calculations $\Delta\nu$ and $\delta\nu$, respectively, for the $F_z(z)$ calculations, while the dashed line and triangles correspond to $F_z(\phi, z)$ calculations of $\Delta\nu$ and $\delta\nu$, respectively. From Table I it is clear that the square-root dependence of $\delta\nu$ on field strength is a consequence of field inhomogeneity: as the field becomes homogeneous in the simulation, β approaches unity. Additionally, the simulations indicate that the $\frac{1}{2}$ value of β is primarily associated with the radial and angular field variations, and also that the $\frac{1}{2}$ value of β is more tightly coupled to the angular field variations than to the radial field variations (i.e., in the simulation where the radial field variations are removed, β only increases by 0.04, but when the angular field variations are removed, β increases by 0.17). Given that the field node implies a strong degree of field inhomogeneity, these observations are consistent with the hypothesis that the course of the saturated line shape's non-Lorentzian character is somehow associated with nodes in the field distribution.

With this hypothesis, one would argue that the angular field variation is particularly important in determining the value of β , since this spatial variation yields a nodal plane for the field. The radial field variation might be viewed as somewhat less important, since it only results in a modal field line. Both transverse variations could, however, be expected to yield significant departures from the predictions of the Karplus-Schwinger theory. Alternatively, since the field

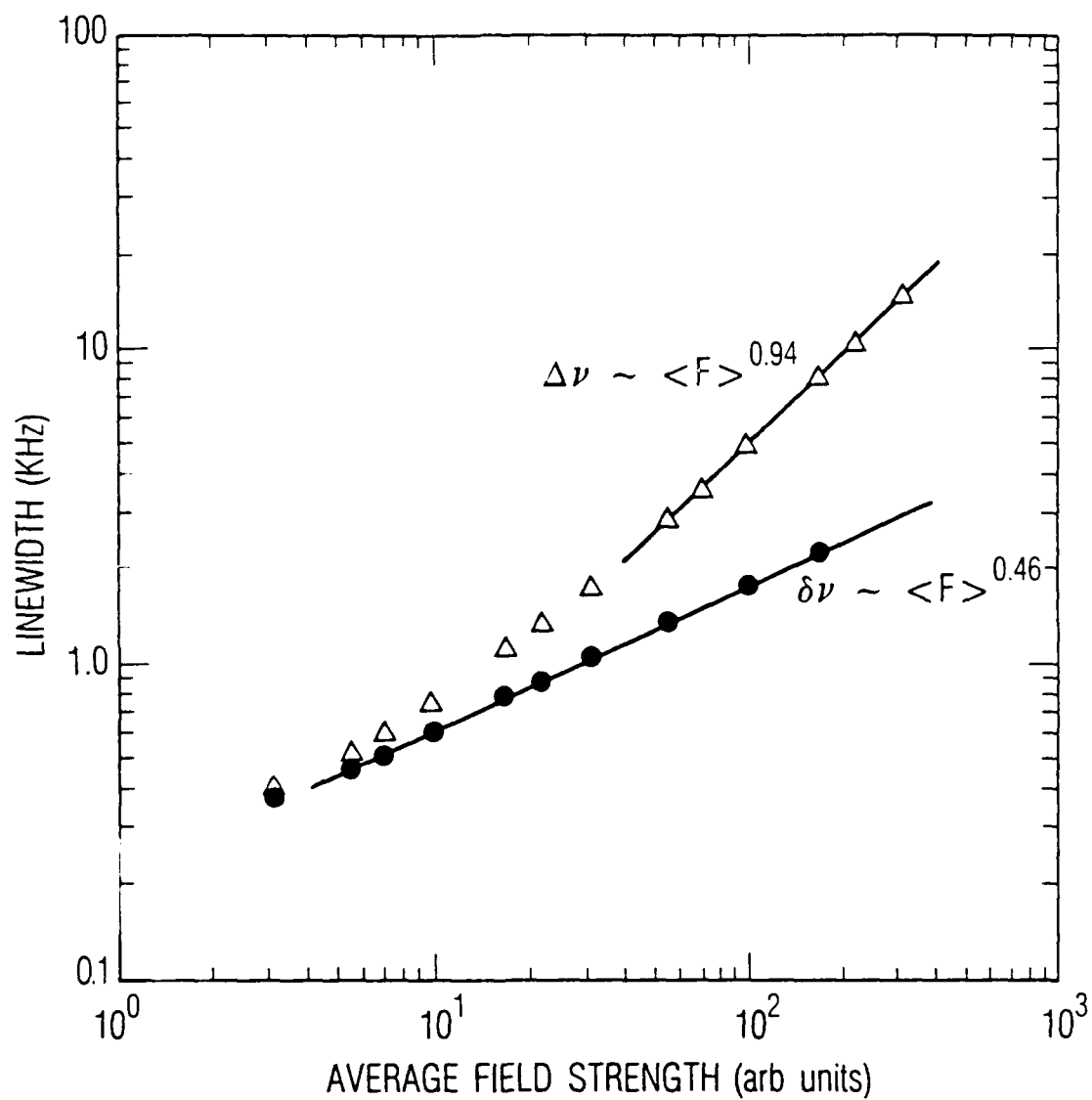


Figure 6. Plot of the theoretical HWHM ($\Delta\nu$) and effective linewidth ($\delta\nu$) vs the average field strength (F). The calculation is for the specific case of a TE_{111} mode field geometry, as was used in the experiment. The numerical data were fit to power-law scaling relations to determine the values of the exponents shown in the figure.

nodes arising from the axial variations occur at the cavity boundaries, where no resonance signal is generated due to the strongly relaxing wall collisions, one would not expect axial variations to significantly alter the $\beta=1$ prediction of the Karplus-Schwinger theory.

Table I. Linewidth power-law exponents for different saturating electromagnetic field geometries: $\Delta\nu \sim \langle F \rangle^\alpha$, $\delta\nu \sim \langle F \rangle^\beta$. In the calculations, the field was allowed to vary over the given spatial dimensions.

Condition	α	β
Experiment	0.93	0.57
TE ₁₁₁ mode calculation: $F_z(r, \phi, z)$	0.94	0.46
TE ₁₁₁ mode calculation: $F_z(\phi, z)$	0.90	0.50
TE ₁₁₁ mode calculation: $F_z(r, z)$	0.89	0.63
TE ₁₁₁ mode calculation: $F_z(z)$	0.98	0.84
TE ₀₁₁ mode calculation: $F_z(r, z)$	0.80	0.45
Analytic analysis		0.50

If this conjecture on the role of field nodes is correct, it should be possible to make qualitative predictions on the value of b for field geometries other than the TE₁₁₁ mode. Consequently, in our final numerical simulation, we considered a field geometry corresponding to a TE₀₁₁ cavity mode, which differs in basically two ways from the TE₁₁₁ cavity mode: (i) as shown in Figure 2(a), the radial nodes of the TE₀₁₁ mode (axial field component) are at $r > 0$, so that there is a nodal surface in the cavity due to the radial field distribution; and (ii) the axial field component of the TE₀₁₁ mode has azimuthal symmetry. For both cavity modes, however, the axial field components exhibit the same axial variation of $\sin(pz/L)$. If the field node conjecture were true, one would expect to obtain a value of b from the simulation roughly equal to 0.5, and as recorded in Table I, this was indeed the case. The numerical simulations thus strongly suggest that field nodes somehow lead to significant deviations from the Karplus-Schwinger theory of saturation broadening, and in the next section the specific role of field nodes in this regard will be addressed.

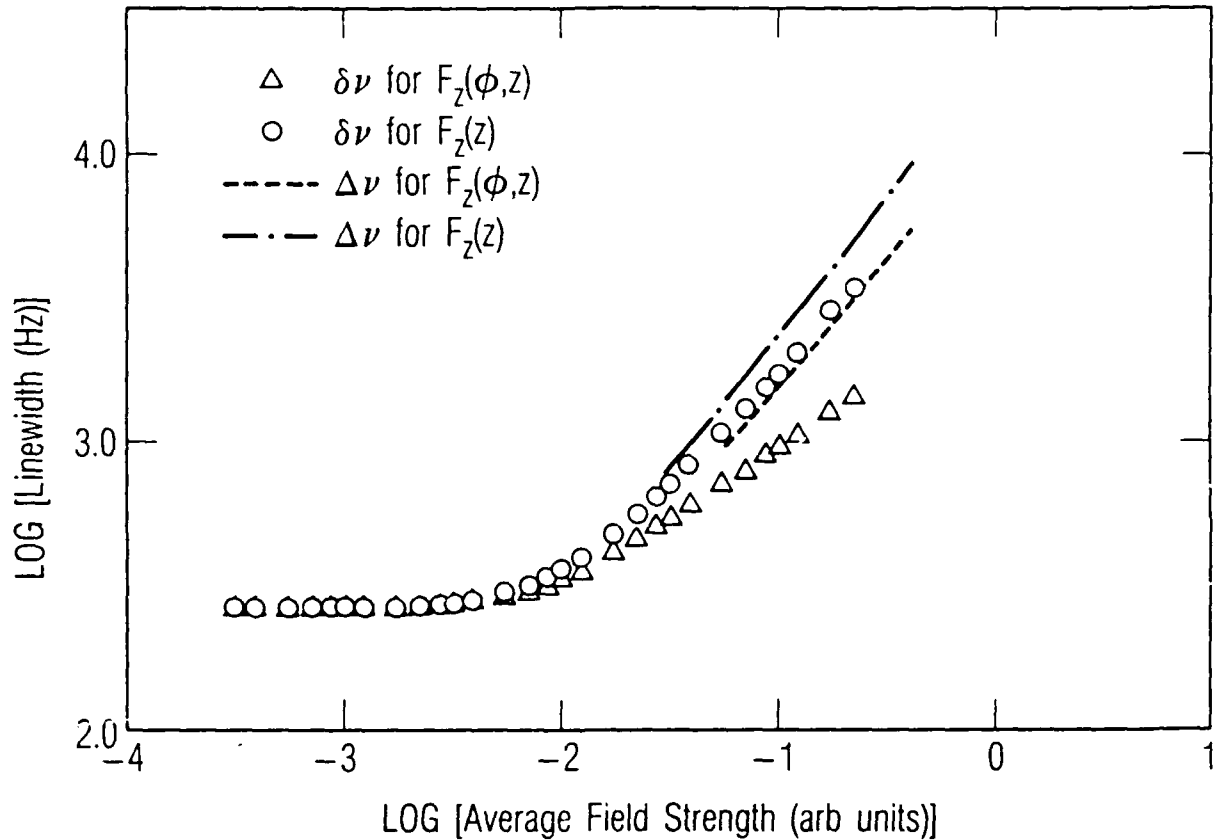


Figure 7. Plot of the theoretical HWHM ($\Delta\nu$) and effective linewidth ($\delta\nu$) vs the average field strength $\langle F \rangle$. The dotted-dashed line and circles correspond to $\Delta\nu$ and $\delta\nu$ calculations, respectively, for the fictitious $\text{TE}_{111} F_z(z)$ mode; the dashed line and triangles correspond, respectively, to $\Delta\nu$ and $\delta\nu$ calculations for the fictitious $\text{TE}_{111} F_z(\phi, z)$ mode. The numerical data were fit to power-law scaling relations to determine the values of the exponents given in Table I.

IV. ANALYTIC APPROXIMATION

In order to gain physical insight into the behavior of $\delta\nu$, which is the quantity of spectroscopic importance, we will consider in this section the one-dimensional problem of an ensemble of two-level atoms interacting with an inhomogeneous saturating electromagnetic field as illustrated in Figure 8. We assume that the spatial motion of the atoms is "slow," so that during a time interval on the order of the atom's dephasing time, the atom interacts with the strong field only in some small localized region. Thus, the signal as a function of field frequency is just the integral of the one-dimensional signal density $s(\nu, x)$:

$$S(\nu) = 2 \int_0^x s(\nu, x) dx . \quad (5)$$

Additionally, we will allow the equilibrium population difference between the two levels ($N_1 - N_2$) (i.e., the population difference between the two levels in the absence of any field) to be a function of position. Thus, taking the observed signal to be proportional to the increased population in the excited state, and assuming that on the local (microscopic) level the Karplus-Schwinger theory is appropriate for describing the strong-field interaction of the atoms, we have

$$S(\nu) = 2 \int_0^x \frac{\Delta n(x) \omega_1^2(x)}{[\gamma^2 + \omega_1^2(x) + (\nu - \nu_0)^2]} dx, \quad (6a)$$

$$\Delta n(x) = n_1^e(x) - n_2^e(x) , \quad (6b)$$

where $n_i^e(x)$ is the equilibrium population density in the i^{th} state at the position x ; $\omega_1(x)$ is the Rabi frequency at the position x , which specifies the local strength of the field-atom interaction [$\omega_1(x) = \mu F(x)/\hbar$]; and ν_0 is taken to be independent of x (no inhomogeneous broadening²⁴). It is clear that given the form of Eq. (6a), saturated resonances with Lorentzian line shapes need not be observed experimentally, except under very special circumstances. Consequently, in order to characterize line shape sharpness, we again employ the effective linewidth $\delta\nu$, which is related to the resonance line shape's second derivative through Eq. (2).

Rewriting and differentiating Eq. (6a) with respect to frequency, we find that

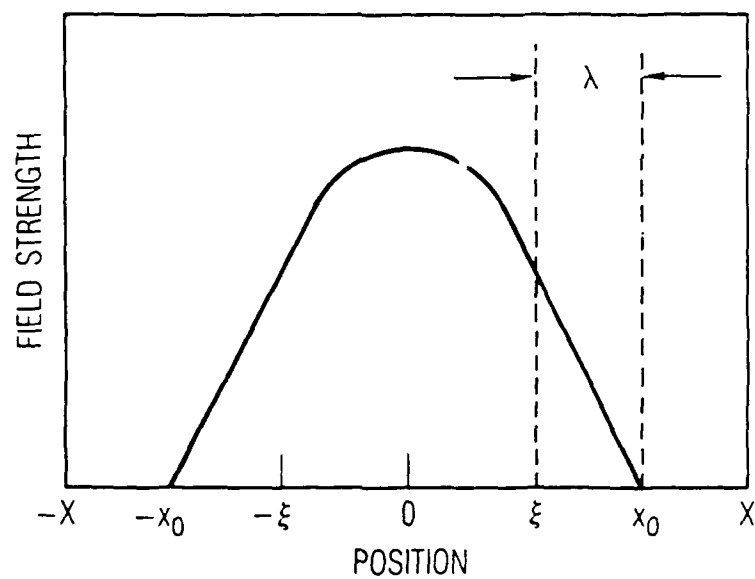
$$S(\nu_0) = 2 \int_0^x \Delta n(x) \omega_1^2(x) / [\gamma^2 + \omega_1^2(x)] dx , \quad (7a)$$

and

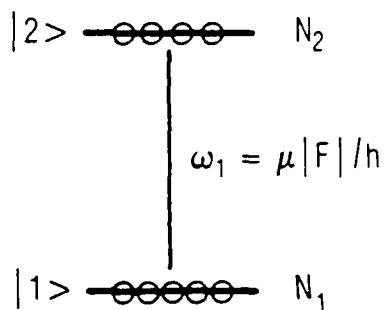
$$S''(\nu_0) = -4 \int_0^x \Delta n(x) \omega_1^2(x) / [\gamma^2 + \omega_1^2(x)]^2 dx . \quad (7b)$$

Note that if the Rabi frequency is independent of x , then

$$\delta\nu = (\gamma^2 + \omega_1^2)^{1/2} = \Delta\nu , \quad (8)$$



(a)



(b)

Figure 8. (a) One-dimensional field geometry used in the analytic analysis of saturation broadening by inhomogeneous fields. The quantities x_0 , ξ , and λ are described in the text. (b) Energy-level diagram of the simple two-level quantum system used in the analytic analysis.

and the effective linewidth increases in proportion to the field strength (when $\omega_1 \gg \gamma$), as expected for a homogeneous field. In the case where the Rabi frequency is not constant, however, the functional relationship between $\delta\nu$ and field strength is much less transparent.

To obtain such a relationship, the first task is to compute $S(\nu_0)$, and we begin by defining the ensemble average equilibrium population difference between the two atomic states,

$$\langle \Delta N \rangle = \int_0^x \Delta n(x) dx . \quad (9)$$

One then finds that

$$S(\nu_0) = 2\langle \Delta N \rangle - 2\gamma^2 \int_0^x \Delta n(x) / [\gamma^2 + \omega_1^2(x)] dx . \quad (10)$$

We next define a position $x_0 - \lambda = \xi$ in the field such that the Rabi frequency at this position equals the atomic relaxation rate [i.e., $\omega_1(x = \xi) = \gamma$]. In this way, we have the general condition that

$$\text{if } |x| < |\xi| \text{ then } \omega_1(x)/\gamma > 1$$

and

$$\text{if } |x| > |\xi| \text{ then } \omega_1(x)/\gamma < 1 .$$

Splitting the integral of Eq. (10) into two parts, corresponding to the two different spatial regions defined above, we have

$$\begin{aligned} S(\nu_0) = & 2\langle \Delta N \rangle - 2\gamma^2 \int_0^\xi \Delta n(x) / [\gamma^2 + \omega_1^2(x)] dx \\ & - 2\gamma^2 \int_\xi^x \Delta n(x) / [\gamma^2 + \omega_1^2(x)] dx . \end{aligned} \quad (11)$$

Here, the first integral accounts for the signal generated in the saturated spatial region of the ensemble, and the second integral accounts for the signal generated in the unsaturated region. Note that the first integral contains terms of order $[\gamma/\omega_1(x)]^2$ or higher, so that the magnitude of this term will be dominated by the spatial region where $\omega_1 \sim \gamma$. If the spatial extent of this region is relatively small, then the first integral makes a negligible contribution to the signal amplitude, and we have

$$S(\nu_0) \approx 2\langle \Delta N \rangle - 2\gamma^2 \int_\xi^x \Delta n(x) / [\gamma^2 + \omega_1^2(x)] dx . \quad (12)$$

Physically, Eq. (12) indicates that the shape of the saturated resonance near line center is dominated by the unsaturated spatial region of the ensemble.

We can narrow the limits of integration in Eq. (12) further by noting that for $x > x_0$, the Rabi frequency is zero. Thus, by defining a term Λ ,

$$\Lambda \equiv \langle \Delta N \rangle \int_{x_0}^x \Delta n(x) dx , \quad (13)$$

we have finally

$$S(v_0) \approx 2\Lambda - 2\gamma^2 \int_{\xi}^{x_0} \Delta n(x) / [\gamma^2 + \omega_1^2(x)] dx. \quad (14)$$

To proceed further, we write the Rabi frequency as the product of the average field strength $\langle F \rangle$ and a function describing the spatial distribution of the field $f(x)$:

$$\omega_1(x) = (\mu/h) \langle F \rangle f(x) , \quad (15a)$$

$$\int_0^x f(x) dx / X \approx 1 . \quad (15b)$$

Expanding $\omega_1(x)$ in a Taylor series about x_0 , we then have

$$\omega_1(x) = (\mu/h) \langle F \rangle [f(x_0) + (x - x_0) f'(x_0) + \dots] . \quad (16)$$

For the case where x_0 corresponds to a node in the field strength distribution, as in the case considered here,

$$\omega_1(x) \approx (\mu/h) \langle F \rangle (x - x_0) \eta , \quad (17)$$

and as a consequence

$$\lambda \approx -h\gamma / (\mu \langle F \rangle \eta) , \quad (18)$$

where $\eta \equiv f'(x_0)$ (evaluated in the case of Fig. 8 from the direction of increasing $|x|$). The value of λ (i.e., the spatial extent of the unsaturated signal region), and hence the range of integration in Eq. (14), is thus found to be a monotonically decreasing function of the average field strength. Physically this corresponds to the fact that as the field strength increases, the unsaturated spatial region of the ensemble decreases in size. It is this phenomenon that has important consequences for the shape of saturated resonances when the saturating field is inhomogeneous.

If we now assume that $\Delta n(x)$ is a slowly varying function of position over the range $\xi < x < x_0$, then we can replace $\Delta n(x)$ by its value at x_0 . The resulting integral is easily evaluated, and we find that

$$S(v_0) \approx 2\Lambda - \pi h \gamma \Delta n(x_0) / 2\mu \langle F \rangle \eta . \quad (19)$$

The evaluation of $S''(v_0)$ proceeds along very similar lines, yielding

$$S''(\nu_0) \approx -(2\pi + 2)h\Delta n(x_0)/2\mu(F)\eta\gamma . \quad (20)$$

Thus, using Eqs. (19) and (20) in Eq. (2), we obtain the effective linewidth $\delta\nu$ in the case of an inhomogeneous saturating field,

$$\delta\nu \approx \sqrt{2\gamma/(3\pi + 2)} [4\Lambda\mu(F)\eta/h\Delta n(x_0) - \pi\gamma]^{1/2} , \quad (21)$$

which yields in the limit of very strong fields

$$\delta\nu \sim (F)^{0.5} . \quad (22)$$

This result is exactly the line-shape behavior that we were attempting to explain. From the above derivation, it is now clear that deviations from the Karplus-Schwinger prediction of $\beta = 1$ arise because the line shape near line center is dominated by the unsaturated atomic population, and because the spatial region containing this population shrinks in size as the average field strength increases. With regard to $\Delta\nu$, since the above derivation suggests that *saturated* atomic population contributes primarily to the wings of the line shape, one would expect $\alpha > 0.5$.

V. SUMMARY

In this report, we have examined the line shape of saturated resonances when the atoms cannot motionally average an inhomogeneity that may be present in the saturating field. The results of this study show that under these conditions, the saturated line shape is non-Lorentzian, and that the central portion of the resonance is primarily determined by those spatial regions of the field where the atoms are not yet saturated. Consequently, the observed resonance line shape is sharper than would be expected from the Karplus-Schwinger theory. By defining an effective linewidth $\delta\nu$, which is the linewidth of a Lorentzian that approximates the central portion of the resonance, the line shape's sharpness can be quantified and examined as a function of saturating field strength (i.e., $\delta\nu \sim \langle F \rangle^\beta$). For the specific case of nodes in the field's spatial distribution, we find that $\beta \sim 0.5$, as opposed to $\beta = 1.0$, which is the value expected from the Karplus-Schwinger theory.

These results have important consequences for precision spectroscopy, especially in the area of atomic clocks, where atomic signals are generated throughout the volume of some microwave cavity. Since the ability to find resonance line center can be quantified by a parameter which is inversely proportional to the effective linewidth,²⁵ the above results suggest that precision spectroscopy may not be as adversely affected by high intensity, inhomogeneous fields as one might expect given the Karplus-Schwinger theory, i.e., for an inhomogeneous field with a node $[S''(\nu_0)]^{1/2} \sim 1/(F)^{1/2}$. For example, with a homogeneous field, the Karplus-Schwinger theory predicts that an increase in radiation intensity (i.e., field energy) of 100 results in a factor of 10 loss in the ability to find resonance line center; however, if an inhomogeneous field has a node in its spatial distribution, then a 10^4 increase in radiation intensity is required in order to degrade this spectroscopic ability by the same factor of 10. (Of course, in this simple example, we have ignored the question of ac Stark and Bloch-Siegert shifts, which is an entirely different aspect of the inhomogeneous-field problem in spectroscopy.²⁴)

In one sense then, the above results indicate a further important restriction on the validity of the Karplus-Schwinger theory of saturation broadening. Regarded in a broader context though, the above results can be seen as an example of a class of phenomena that arises when one studies the field-atom interaction with real fields. Real fields are never perfectly homogeneous, and the inhomogeneity can have important consequences for the outcome of many field-atom interaction experiments. In this regard, it is worth noting that spatial field variations can play an important role in photoionization experiments, and caution must be exercised in the evaluation of multiphoton ionization cross sections in the absence of field inhomogeneity information.^{26,27} In this broader context, the present results similarly indicate how microscopic field-atom interactions are not always simply reflected in macroscopic experimental line shapes, when field inhomogeneities are present.

REFERENCES

1. C. H. Townes, *Phys. Rev.* **70**, 665 (1946).
2. R. Karplus and J. Schwinger, *Phys. Rev.* **73**, 1020 (1948).
3. H. S. Snyder and P. I. Richards, *Phys. Rev.* **73**, 1178 (1948).
4. It should be noted that it is often important to introduce a distinction between power and saturation broadening. For a discussion of these distinctions, see, for example, R. A. Van Calcar, M. J. G. Heuts, B. K. Van Uitert, H. A. J. Meijer, T. J. Hollander, and C. Th. J. Alkemade, *J. Quant. Spectrosc. Radiat. Transfer* **28**, 1 (1982).
5. V. S. Lisitsa and S. I. Yakovlenko, *Zh. Eksp. Teor. Fiz.* **68**, 479 (1975) [*Sov. Phys. — JETP* **41**, 233 (1975)].
6. Y. Rabin, D. Grimbirt, and S. Mukamel, *Phys. Rev. A* **26**, 271 (1982).
7. M. L. Citron, H. R. Gray, C. W. Gabel, and C. R. Stroud, *Phys. Rev. A* **16**, 1507 (1977).
8. A. R. D. van Bergen, T. J. Hollander, and C. Th. J. Alkemade, *J. Quant. Spectrosc. Radiat. Transfer* **33**, 419 (1985).
9. T. Endo, T. Muramoto, and T. Hashi, *Opt. Commun.* **51**, 163 (1984).
10. N. D. Bhaskar, J. Camparo, W. Happer, and A. Sharma, *Phys. Rev. A* **23**, 3048 (1981).
11. J. C. Camparo and R. P. Frueholz, *Phys. Rev. A* **31**, 1440 (1985); **32**, 1888 (1985).
12. R. H. Dicke, *Phys. Rev.* **89**, 472 (1953); R. P. Frueholz and C. H. Volk, *J. Phys. B* **18**, 4055 (1985).
13. J. C. Camparo, *Contemp. Phys.* **26**, 443 (1985).
14. W. Happer, *Rev. Mod. Phys.* **44**, 169 (1972).
15. J. D. Jackson, *Classical Electrodynamics* (Wiley, New York, 1975), pp. 356–360.
16. F. A. Franz and C. Volk, *Phys. Rev. A* **14**, 1711 (1976).
17. P. Minguzzi, F. Strumia, and P. Violino, *Nuovo Cimento B* **46**, 145 (1966).
18. J. C. Camparo and R. P. Frueholz, *J. Appl. Phys.* **59**, 301 (1986).
19. J. C. Camparo and R. P. Frueholz, *J. Appl. Phys.*, **59**, 3313 (1986).
20. J. C. Camparo and R. P. Frueholz, *IEEE Trans. Ultrasonic. Ferroelec. Freq. Control* **UFFC-34**, 607 (1987).
21. J. C. Camparo and R. P. Frueholz, *IEEE Trans. Ultrasonic. Ferroelec. Freq. Control* (to be published).
22. As discussed in Ref. 11, the saturated linewidths in this multilevel system will in general be larger than the Rabi frequency. However, the scaling factor is a constant, and

does not affect the functional relationship between the saturated linewidth and the magnitude of the saturating field strength.

23. For a discussion of the laws of Bouger, Lambert, and Beer and how they differ, see J. H. Goldstein and R. A. Day, *J. Chem. Educ.* **31**, 417 (1954); D. F. Swinehart, *ibid.* **39**, 333 (1962), and references therein.
24. J. C. Camparo, R. P. Frueholz, and C. H. Volk, *Phys. Rev. A* **27**, 1914 (1983).
25. J. C. Camparo, R. P. Frueholz, and C. M. Klimcak, *Phys. Rev. A* **36**, 2072 (1987).
26. L. Chin and N. R. Isenor, *Can. J. Phys.* **48**, 1445 (1970).
27. P. Lambropoulos, *Phys. Lett.* **40A**, 199 (1972).

LABORATORY OPERATIONS

The Aerospace Corporation functions as an "architect-engineer" for national security projects, specializing in advanced military space systems. Providing research support, the corporation's Laboratory Operations conducts experimental and theoretical investigations that focus on the application of scientific and technical advances to such systems. Vital to the success of these investigations is the technical staff's wide-ranging expertise and its ability to stay current with new developments. This expertise is enhanced by a research program aimed at dealing with the many problems associated with rapidly evolving space systems. Contributing their capabilities to the research effort are these individual laboratories:

Aerophysics Laboratory: Launch vehicle and reentry fluid mechanics, heat transfer and flight dynamics; chemical and electric propulsion, propellant chemistry, chemical dynamics, environmental chemistry, trace detection; spacecraft structural mechanics, contamination, thermal and structural control; high temperature thermomechanics, gas kinetics and radiation; cw and pulsed chemical and excimer laser development including chemical kinetics, spectroscopy, optical resonators, beam control, atmospheric propagation, laser effects and countermeasures.

Chemistry and Physics Laboratory: Atmospheric chemical reactions, atmospheric optics, light scattering, state-specific chemical reactions and radiative signature of missile plumes, sensor out-of-field-of-view rejection, applied laser spectroscopy, laser chemistry, laser optoelectronics, solar cell physics, battery electrochemistry, space vacuum and radiation effects on materials, lubrication and surface phenomena, thermionic emission, photosensitive materials and detectors, atomic frequency standards, and environmental chemistry.

Computer Science Laboratory: Program verification, program translation, performance-sensitive system design, distributed architectures for spaceborne computers, fault-tolerant computer systems, artificial intelligence, microelectronics applications, communication protocols, and computer security.

Electronics Research Laboratory: Microelectronics, solid-state device physics, compound semiconductors, radiation hardening; electro-optics, quantum electronics, solid-state lasers, optical propagation and communications; microwave semiconductor devices, microwave/millimeter wave measurements, diagnostics and radiometry, microwave/millimeter wave thermionic devices; atomic time and frequency standards; antennas, rf systems, electromagnetic propagation phenomena, space communication systems.

Materials Sciences Laboratory: Development of new materials: metals, alloys, ceramics, polymers and their composites, and new forms of carbon; non-destructive evaluation, component failure analysis and reliability; fracture mechanics and stress corrosion; analysis and evaluation of materials at cryogenic and elevated temperatures as well as in space and enemy-induced environments.

Space Sciences Laboratory: Magnetospheric, auroral and cosmic ray physics, wave-particle interactions, magnetospheric plasma waves; atmospheric and ionospheric physics, density and composition of the upper atmosphere, remote sensing using atmospheric radiation; solar physics, infrared astronomy, infrared signature analysis; effects of solar activity, magnetic storms and nuclear explosions on the earth's atmosphere, ionosphere and magnetosphere; effects of electromagnetic and particulate radiations on space systems; space instrumentation.